 CMES, vol.6, no.2, pp.153-168, 2004

# Large Scale Parallel Simulation and Visualization of 3D Seismic Wavefield Using the Earth Simulator

**T. Furumura**[1] **and L. Chen**[2]

**Abstract:** Recent developments of the Earth Simulator, a high-performance parallel computer, has made it possible to realize realistic 3D simulations of seismic wave propagations on a regional scale including higher frequencies. Paralleling this development, the deployment of dense networks of strong ground motion instruments in Japan (K-NET and KiK-net) has now made it possible to directly visualize regional seismic wave propagation during large earthquakes. Our group has developed an efficient parallel finite difference method (FDM) code for modeling the seismic wavefield and a 3D visualization technique, both suitable for implementation on the Earth Simulator. Large-scale 3D simulations of seismic wave propagation have been conducted using these techniques for recent damaging earthquakes such as the 2000 Tottori-ken Seibu ($M_J$ 7.3) earthquake and the 1993 Kushiro-oki earthquakes ($M_J$ 7.8). Comparison of the simulation results with the dense array observations provides insights into the nature of complex seismic wave propagation through the heterogeneous subsurface structure of Japan. The simulations are in good agreement with the observations in terms of the features of the seismic wavefield, indicating that the simulation is already at a suitable level for use in investigating the expected pattern of ground motions for future earthquake scenarios.

**keyword:** Earth Simulator, Earthquake, Parallel Computing, Seismic Waves, Wave Propagation

## 1 Introduction

The complex source rupture process and heterogeneities in the crust and upper mantle structure form an important control on the regional seismic wavefield, particularly for high-frequency waves over 1 Hz. Small-scale heterogeneities such as sedimentary basins introduce significant amplification of ground motion leading to prolonged ground shaking in these regions. In order to visualize the seismic wave behavior imposed by such heterogeneous structures, and to understand the process of strong motion generation during damaging earthquakes, high-resolution computer simulations including such heterogeneities in the shallow superficial structure are indispensable.

The recent developments of the Earth Simulator, a high-performance parallel computer (640 nodes = 5,120 CPUs, 40 TFlops) at the Japan Marine Science and Technology Center (JAMSTEC), have made it possible to realize realistic simulations of 3D seismic wave propagation on a regional scale including higher frequencies. Our group has developed an efficient parallel finite difference method (FDM) code for implementation on the Earth Simulator, along with a suitable volume visualization technique for the 3D wavefield.

The results of the computer simulation can be compared with the dense seismic arrays deployed in Japan, K-NET [Kinoshita (1998)] and KiK-net [Aoi and Fujiwara (1999)], by the National Research Institute for Earth Science and Disaster Prevention (NIED), comprising more than 1,800 stations across Japan (Fig. 1). Detailed comparison of computer simulations with observations is expected to provide a direct means of understanding the nature of the complex seismic wavefield imposed by heterogeneities in the structure.

In this paper, the parallel FDM simulation of seismic waves is introduced, and efficient visualization techniques for illustrating the observed and simulated ground motions and simulated 3D wavefield are presented. Unlike the latest simulation techniques for seismic wavefield modeling, such as based on the Boundary Element Method [e.g., Hatzigeorgiou and Beskos (2002)] and the Meshless Local Petrov-Galerkin (MLPG) Method [e.g., Sellountos and Polyzos (2003); Sladek, Sladek, and

[1] Earthquake Research Institute, University of Tokyo, 1-1-1 Yayoi, Bunkyo-ku 113-0032, JAPAN

[2] Research Organization for Information Sciences and Technology, 2-2-54, Nakamguro, Meguro-ku, Tokyo 153-0061, Japan.

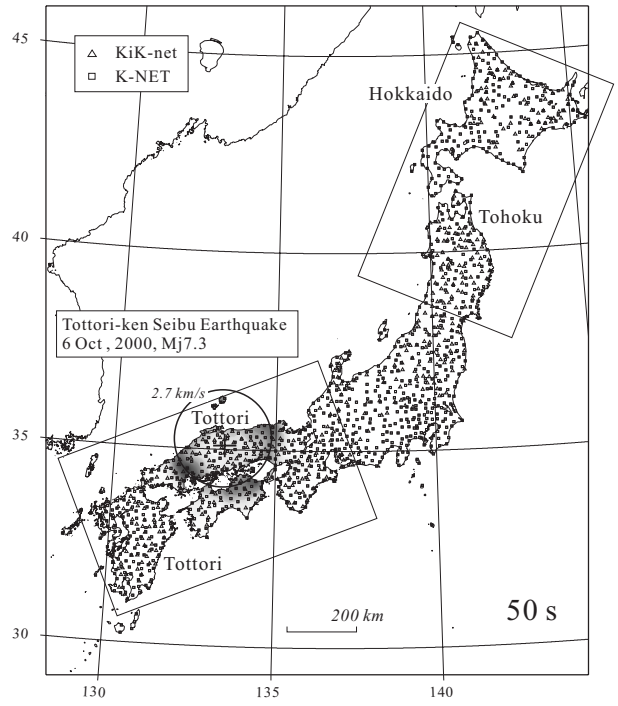


**Figure 1** : Dense network of strong ground motion station across Japan and observed ground motion during the 2000 Tottori-ken Seibu earthquake (50 s after source initiation). Circle indicates the wavefront of wave propagation at 2.7 km/s, and rectangles denote the area of numerical simulation for western and northern Japan.

Zhang (2003)], the efficiency of the parallel FDM has already been demonstrated clearly on many parallel computers such as for a SMP machine and for a cluster of massive processors [e.g., Olsen, Archuleta, and Matares (1995); Furumura, Koketsu, and Wen (2002)]. Two examples of computer simulations using the Earth Simulator are then demonstrated. The first simulation models the long-period surface wave (Love wave) propagation during the 2000 Tottori-ken Seibu earthquake ($M_J$ 7.3) in western Japan, showing the amplification effects of long-period ground motions in sedimentary basins. The second example considers the cause of the anomalous seismic intensity pattern for deep plate earthquakes in northern Japan. This latter example is well observed by the dense seismic array across Japan, and the series of computer simulations reveals the contribution of the subducting plate to the efficient transmission of high-frequency waves over 2 Hz.

## 2 Numerical Simulation of Seismic Wave Propagation

This section provides a brief review of the simulation of seismic wave propagation based on the solution of equations of motion.

### 2.1 Equations of Motion for 3D Seismic Wavefields

The seismic wavefield in the 3D Cartesian coordinate system is expressed by equations of motion as

$$\rho \ddot{u}_p = \frac{\partial \sigma_{xp}}{\partial x} + \frac{\partial \sigma_{yp}}{\partial y} + \frac{\partial \sigma_{zp}}{\partial z} + f_p, \quad (p = x,y,z), \quad (1)$$

where $\sigma_{pq}$, $f_p$ and $\rho$ are stress, body force and density, and $\ddot{u}_p$ represents particle acceleration. The stresses in an isotropic elastic medium are given by

$$\sigma_{pq} = \lambda(e_{xx} + e_{yy} + e_{zz})\delta_{pq} + 2\mu e_{pq}, \quad (p,q = x,y,z), \quad (2)$$

with the Lamé's constants $\lambda$ and $\mu$. The strains are defined by

$$e_{pq} = \frac{1}{2}\left(\frac{\partial u_p}{\partial q} + \frac{\partial u_q}{\partial p}\right), \quad (p,q = x,y,z). \quad (3)$$

With the increment of time of Eq. (1), the velocity at the next time-step $t = (n+1/2)\Delta t$ is calculated by integration with time step $\Delta t$ as follows.

$$\dot{u}_p^{n+\frac{1}{2}} = \dot{u}_p^{n-\frac{1}{2}} + \frac{1}{\rho}\left(\frac{\partial \sigma_{px}^n}{\partial x} + \frac{\partial \sigma_{py}^n}{\partial y} + \frac{\partial \sigma_{pz}^n}{\partial z} + f_p^n\right)\Delta t, \quad (4)$$

where $\dot{u}_p^{n\pm\frac{1}{2}}$ is the particle velocity at time $t = (n \pm \frac{1}{2})\Delta t$. Differentiation of Eqs. (2) and (3) with respect to time yields

$$\sigma_{pq}^{n+1} = \sigma_{pq}^n + \left[\lambda\left(\frac{\partial \dot{u}_x^{n+\frac{1}{2}}}{\partial x} + \frac{\partial \dot{u}_y^{n+\frac{1}{2}}}{\partial y} + \frac{\partial \dot{u}_z^{n+\frac{1}{2}}}{\partial z}\right)\delta_{pq} + \mu\left(\frac{\partial \dot{u}_p^{n+\frac{1}{2}}}{\partial q} + \frac{\partial \dot{u}_q^{n+\frac{1}{2}}}{\partial p}\right)\right]\Delta t, \quad (p,q = x,y,z). \quad (5)$$

The absorbing boundary of Cerjan, Kosloff, Kosloff, and Reshef (1985) is applied at the 20th grid point in the area surrounding the 3D model in order to reduce artificial reflections. The zero-stress boundary conditions of Graves (1996) are also applied to the stress components $\sigma_{zp}$ in Eq. (2) at the free surface. Anelastic attenuations of the P and S waves ($Q_P$ and $Q_S$) are incorporated in the time-domain simulation by introducing appropriate dampers to Eq. (5) [see Hestholm (1999)].

### 2.2 Spatial Differentiation by FDM and PSM

The spatial derivatives in Eqs. (4) and (5) can be calculated by FDM, or more accurately by fast Fourier transform (FFT) using the Fourier spectral method (PSM).

#### 2.2.1 Spatial Differentiation by FDM

The spatial derivatives of the sequence of data $f(l\Delta x), (l = 1,2,..,N)$ to be differentiated with respect to $x$ are obtained by means of a centered, staggered-grid FDM as given by

$$\frac{d}{dx}f(n\Delta x) = \frac{1}{\Delta x}\sum_{m=1}^{M/2} c_m [f\{x+(m+1/2)\Delta x\} - f\{x-(m-1/2)\Delta x\}], \quad (6)$$

where $c_m, (m = 1,2,...,M/2)$ are the weights of the centered staggered-grid FDM of order $M$, as listed in Tab. 1. Although the accuracy of the FDM increases steadily with increasing length of FDM operators, so does the computational time.

**Table 1** : Weights for a centered staggered-grid FDM of order M.

| M | $c_1$ | $c_2$ | $c_3$ | $c_4$ |
|---|---|---|---|---|
| 2 | 1 | | | |
| 4 | 9/8 | -1/24 | | |
| 8 | 1255/1024 | -245/3072 | 49/5120 | -5/7168 |

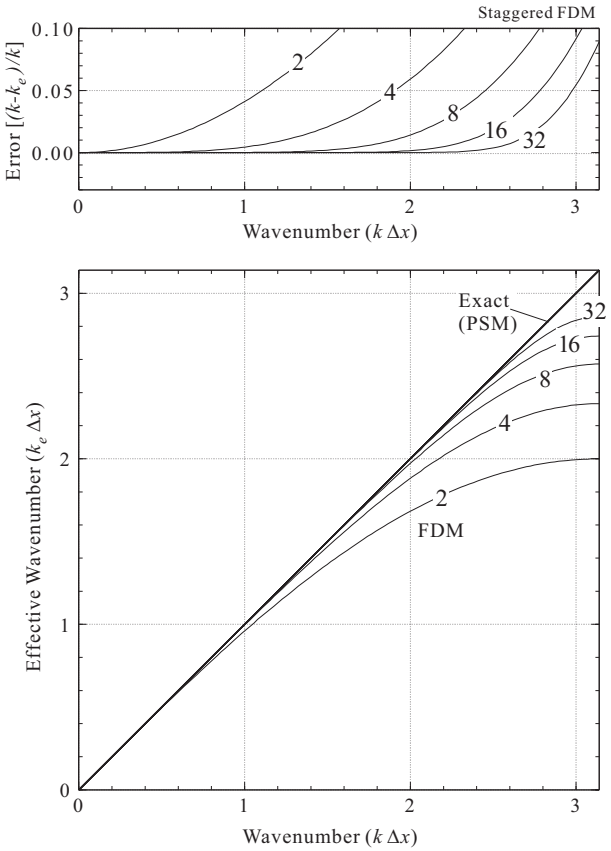


**Figure 2** : Plot of the effective wavenumber for first-derivative FDM approximations of order 2, 4,..., 32, and for exact differentiation by PSM (thick line), with the corresponding numerical error (top).

#### 2.2.2 Accurate Differentiation Using the FFT

An alternative and attractive approach to higher-order FDM calculation is to use the FFT to achieve differentiation analytically in the wavenumber domain. The data $f(l\Delta x)$ to be differentiated can be expanded in the wavenumber domain by discrete sine and cosine polynomials using the FFT for real-valued data (RFFT) as follows.

$$f(n\Delta k) = \sum_{l=0}^{N/2} A(l\Delta k)\cos(2\pi nl/N) + \sum_{l=1}^{N/2} B(l\Delta k)\sin(2\pi nl/N), \quad (7)$$

where $A$ and $B$ are the cosine and sine coefficients of the RFFT for $f$, and $\Delta k$ is the discrete wavenumber given by $\Delta k = 2\pi/(N\Delta x)$. The derivative of $f$ in the wavenumber domain is calculated by multiplying by the discrete wavenumbers $l\Delta k$ and involving a phase advance of $90^\circ$ in the equation (or equivalently, exchanging $A$ and $B$ with $-B$ and $A$), followed by transformation back into the physical domain using the RFFT inverse transform, which is given by

$$\frac{d}{dx}f(n\Delta x) = \sum_{l=1}^{N/2-1} (l\Delta k)B(l\Delta k)\cos(2\pi nl/N) + \sum_{l=1}^{N/2-1} (-l\Delta k)A(l\Delta k)\sin(2\pi nl/N). \quad (8)$$

The differentiation using the FFT in Eq. 8 is equivalent to that using the highest ($N$-th) order FDM for Eq. 6, but with a much lower computational cost in the multiplication and summation calculations. Thus, the PSM has long been applied as an alternative to higher-order FDM

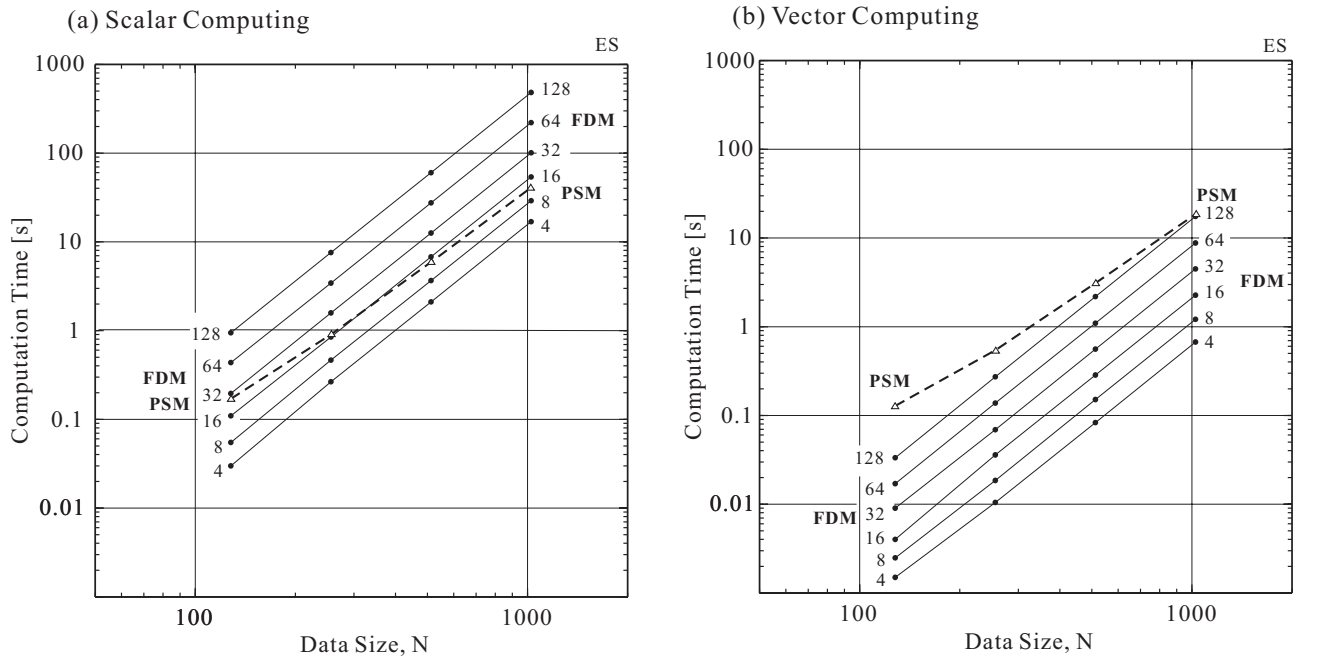


**Figure 3** : Computation time for FDM (solid lines) and PSM modeling (dashed line) on the Earth Simulator as a function of data size and order of the FDM (4,8,...,128) by (a) scalar computing without utilizing vector hardware, and (b) ordinary vector computing.

for large-scale 3D simulations of seismic wave propagation using clusters of personal computers (PCs) and workstations [e.g., Reshef, Kosloff, Edwards, and Hsiung (1988); Furumura, Kennett, and Takenaka (1998)].

### *2.3 Accuracy of Higher-order FDM and PSM*

The accuracy of spatial differentiation by FDM is often evaluated roughly by Fourier analysis of a periodic function of wavenumber $k$, as follows.

$$f(n\Delta x) = \exp(\mathrm{i}kn\Delta x). \tag{9}$$

The derivative of the function is obtained analytically as

$$\frac{d}{dx}f(n\Delta x) = \mathrm{i}k_e \exp(\mathrm{i}kn\Delta x), \tag{10}$$

where $k_e$ is the effective wavenumber, with $k_e = k$ in the analytical differentiation. The approximate first derivative of the function by the second-order staggered-grid central FDM can be written as

$$\begin{aligned}\frac{d}{dx}f(n\Delta x) &= \frac{1}{\Delta x}[\exp\{\mathrm{i}k(n\Delta x + 1/2\Delta x)\} \\ &\quad - \exp\{\mathrm{i}k(n\Delta x - 1/2\Delta x)\}] \\ &= \mathrm{i}\frac{\sin(k\Delta x/2)}{\Delta x/2}f(n\Delta x),\end{aligned} \tag{11}$$

The numerical differentiation then shows that $k_e = \sin(k\Delta x/2)/(\Delta x/2)$.

A plot of the effective wavenumber for the second-order centered staggered-grid FDM is presented in Fig. 2 along with the higher-order (4, 8,..., 32nd) schemes. It is evident that the effective wavenumber of the FDMs with order of 16 or higher is close to the exact differentiation. The error in the effective wavenumber is less than 1% over a progressively larger wavenumber range from 0 to about $\pi \times 2/3$, corresponding to seismic waves with wavelengths of 3 $\Delta x$ or longer. Therefore, higher-order FDM (order 16 or higher) approximations can calculate seismic wave propagation at three grid samples per shortest wavelength with a small grid dispersion error less than 1%. However, such a larger grid model may cause an undersampling problem when modeling heterogeneous structures because a smooth interface in the heterogeneous structure become blocky and step-like structure.

### *2.4 Computation Speed of FDM and PSM*

As calculation of the 18 spatial derivatives appearing in Eq. 4 and Eq. 5 accounts for more than 80–90% of the total computational cost of 3D modeling, the most crucial

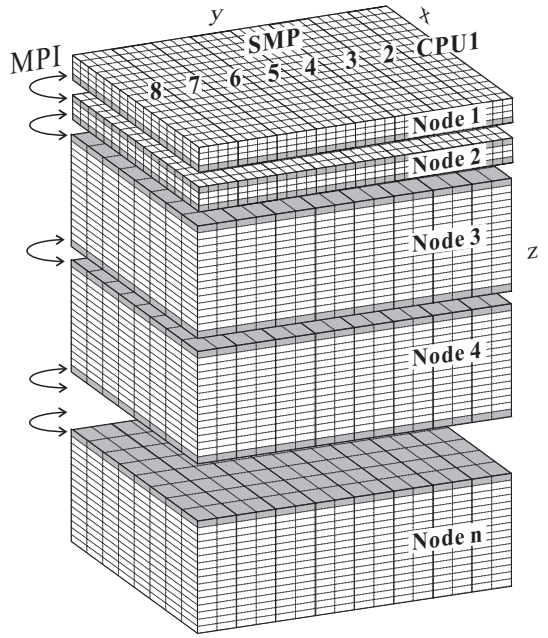


**Figure 4** : Multigrid FDM model for 3D simulation of seismic wave propagation. An SMP/MPI hybrid parallel algorithm is used for parallel computing.

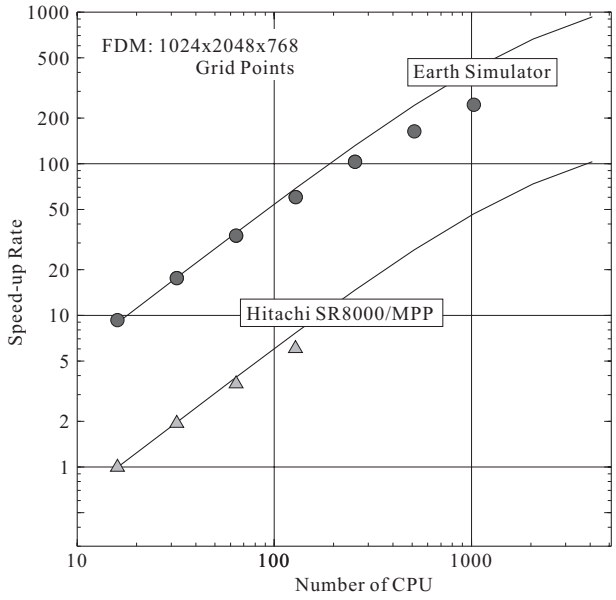


**Figure 5** : Speed-up of parallel FDM simulation using the Earth Simulator and Hitachi SR8000/MPP as a function of processor number. Solid lines are the expected speed-up rate by theoretical experiments.

factor in maintaining high levels of computational performance on the Earth Simulator is the efficient choice of differentiation scheme.

As mentioned above, the PSM has long been recognized as a very efficient alternative to higher-order FDMs, and PSM have been used by our group for large-scale parallel simulation of seismic waves using scalar computers such as clusters of PCs [Furumura, Kennett, and Takenaka (1998)]. This is also the case for the Earth Simulator if the vector hardware of the machine is not utilized [Fig. 3(a)]. However, by making full use of the vector hardware, a significant speed improvement in the FDM simulation can be achieved [Fig. 3(b)]. Vector computing does not provide as much benefit for FFTs, even special FFTs that are fully optimized for implementation on the Earth Simulator. Therefore, the authors selected a higher-order FDM for implementation on the Earth Simulator for high-performance computation of seismic waves instead of the PSM.

## 3 Parallel Simulation of 3D Seismic Wavefield on the Earth Simulator

Parallel simulation of seismic wavefields is achieved by partitioning the 3D model and assigning each subdomain to a node of the Earth Simulator to achieve concurrent computing. The 3D model is partitioned vertically into $N_p$ subregions with some overlap between neighboring regions. To allow for the inclusion of small-scale heterogeneities such as shallow basin structures into the main 3D simulation model, a multigrid approach was adopted, embedding a finer mesh model in the coarser main mesh (Fig. 4). Wavefields with different mesh sizes are then linked together by an accurate interpolation procedure based on Fourier polynomial extrapolation [Furumura, Kennett, and Koketsu (2003)]. The message-passing interface (MPI) is employed to exchange data for the overlapping area between neighboring processors.

The Earth Simulator is a distributed-memory parallel machine with 640 supercomputer nodes connected via a fast (12.3 Gbyte/s) single-stage cross-bar network. Each node consists of 8 high-speed (8 GFlops) vector processors with 16 Gbyte of shared memory. For efficient parallel computing using a large number of processors of the distributed-memory/shared-memory parallel (SMP) machine, a hybrid parallel approach was adopted based on thread parallel computing using 8 vector processors on each node with MPI for intra-node parallel computing.

The performance of the parallel FDM simulation can be

roughly estimated based on the data transmission rates ($V_c$ byte/s) between processors and the calculation speed ($V_d$ byte/s) for FDM modeling. For a single-precision (4 bytes/variable) arithmetic calculation, the computation speed can be obtained by measuring the computation time $T_d$ for FDM calculation of a $N_x \times N_y \times N_z$ grid model as follows.

$$V_d = \frac{N_x \times N_y \times N_z \times 4}{T_d}. \tag{12}$$

It is assumed that data transmission for each node pair is performed at $V_c$ byte/s, as estimated from the data transmission time $T_c$ and the data size to be exchanged between neighboring nodes (shaded area in Fig. 4) for 12 variables at each time step:

$$V_c = \frac{N_x \times N_y \times M/2 \times 4}{T_c} \times 12 \tag{13}$$

The parallel performance of the FDM simulation with $N_p$ nodes relative to sequential computation can then be roughly estimated from the ratio of $V_c$ to $V_d$, that is,

$$\begin{aligned} R(N_p) &= \frac{T_d}{T_d/N_p + T_c} \\ &= \frac{N_p}{1 + N_p \times M/N_z \times 6 \times V_d/V_c}, \end{aligned} \tag{14}$$

where $R$ is the expected speed-up rate for $N_p$ nodes, and $M$ is the order of the FDM ($M = 2, 4, 8, ...$) in the vertical direction [see Furumura, Koketsu, and Wen (2002) for details].

Values of $V_c$ and $V_d$ were obtained on the Earth Simulator from simple benchmark test programs using FDM and MPI. The results are listed in Tab. 2. The Earth Simulator was roughly ten times faster for this simulation in terms of both $V_d$ and $V_c$ compared to the same simulation performed on the Hitachi SR8000/MPP at the Supercomputer Center of the University of Tokyo, and markedly faster than a cluster of Intel Xeon PCs over Gigabit Ethernet. Therefore, a good level of speed-up can be expected using a large number of processors on the Earth Simulator, as has already achieved on the SR8000/MPP.

Figure 5 illustrates the speed-up rate of parallel computing using 2 to 128 nodes (16 to 1024 processors) of the Earth Simulator. A good speed-up is achieved with a large number of processors, consistent with the theoretical predictions. The slight difference between the theoretical prediction and this experiment may be due to the overhead of MPI communication and other sequential computations in the parallel simulation. The parallel simulation using 1024 processor of the Earth Simulator runs at a vector operation ratio of 99.68%, with performance of about 3.2 TFlops, approximately 40% of the theoretical peak performance for this number of processors.

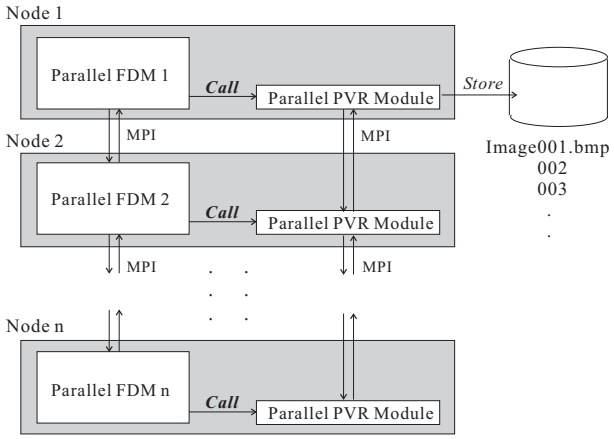


**Figure 6** : Schematic illustration of parallel volume visualization on the Earth Simulator. The FDM program on each node calls the parallel volume rendering (PVR) module at each time step to generate the image by MPI with other PVR modules on neighboring nodes. The PVR module on the master node (Node 1) stores the combined image to hard disk.

## 4 Visualization of 3D Seismic Wavefield

The development of effective visualization techniques for 3D seismic wavefields is a challenging issue, particularly when dealing with the large datasets of high-resolution simulations and dense seismic observations.

Our group has developed a set of efficient techniques in order to understand the complex seismic behavior in heterogeneous structures. One of these visualization techniques is used in the present application to render the 2D wavefield of surface ground motions, which will be useful in both simulation and observation. Another technique used here is based on volume rendering, and is used to visualize the 3D seismic wavefield in large-scale parallel simulations using the Earth Simulator.

The sequence of rendered images at each time step is finally combined into an MPEG movie, which is very useful for interpreting and understanding the complex seis-

**Table 2** : Data communication speed $V_c$ between nodes and computation speed $V_d$ for FDM simulation on various parallel computers.

| Parallel Machines | $V_d$ (Kbyte/s) | $V_c$ (Kbyte/s) | $V_d/V_c$ |
|---|---|---|---|
| The Earth Simulator | 78,910 | 855,200 | 0.0923 |
| Hitachi SR8000/MPP | 7,920 | 85,600 | 0.0925 |
| Intel Xeon (2.2 GHz, DDR266) + GbE | 2,240 | 14,530 | 0.1541 |

mic behavior in heterogeneous structures.

### *4.1 Visualization of Surface Ground Motion*

Ground motions observed as accelerations recorded by K-NET and KiK-net stations are first integrated to construct a velocity record after applying a low-cut filter with a cut-off frequency of 0.05 Hz to remove instrument noise. The ground motion as gridded data is obtained by interpolation of the velocity record using the gridding algorithm of Smith and Wessel (1990).

As the intensity of ground motion and strong motion damages manifests on a logarithmic scale of horizontal ground velocity motion, a scalar value of the strength of the ground motion is calculated from simulated and observed horizontal velocity motion using the following equation.

$$\dot{u}(x,y) = \frac{1}{2}\log\{\dot{u}_x(x,y)^2 + \dot{u}_y(x,y)^2\} \qquad (15)$$

The resulting scalar, which represents the energy of the seismic wave at each point on the regular mesh, is then used to render the wavefront using the "height-field" function of the POV-Ray rendering library. In order to highlight the wavefront of larger ground motions and eliminate weak and scattered wavefields (e.g., less than 0.1% of the peak ground motion), an opacity function proportional to the logarithmic amplitude of the ground motion is applied in the rendering. The figure is protracted onto a surface topography image produced using the same rendering tool in the same viewing coordinates. The resulting combined image increases the confidence of imaging for the regional wavefield and assists in the understanding of localized seismic disturbances in areas such as sedimentary basins. An example is shown in Fig. 8.

### *4.2 Visualization of 3D Wavefield by Concurrent Parallel Volume Rendering*

As the 3D simulation produces huge data sets in each time step, it is difficult to store all of the simulation results on an external hard disk for post processing such as using a volume rendering technique [Levoy (1988)]. Therefore, an efficient concurrent parallel volume rendering (PVR) technique is adopted for 3D wavefield visualization, developed specifically for implementation on the Earth Simulator [Chen, Fujsihiro, and Nakajima (2003)].

This concurrent technique utilizes data stored on the main memory of the Earth Simulator during simulation, unnecessary to save the data to an external hard disk or transfer huge amounts of data to another machines over the network. The main program of the FDM simulation on each node calls the visualization modules at each time step, and the PVR modules generates a frame image from the simulation results held in memory (Fig. 6).

#### *4.2.1 Performance Optimization on the Vector Machine*

Since no graphic libraries such as the OpenGL nor special graphics hardware, such as used for texture mapping, alpha-blending, etc, are available on the Earth Simulator, it is very important to make full use of the computational superiority on the fast arithmetic calculation and large amount of memory on the machine to achieve a good visualization performance. We use the following techniques for the fast visualization:

*(1)Optimization in PVR algorithm: Hybrid image-space and object-space PVR*

Three types of parallelisms occur in existing ray-casting PVR algorithms: image-space parallel, object-space parallel and time-space parallel.

Image-space parallel subdivides the screen into a number of areas, and assigns one or more areas to each CPU, whereas the object-space parallel subdivides the whole

volume data into a number of subvolumes, and assigns one or more subvolumes to each CPU. Image-space parallel makes load balance easy to obtain and involves less communication, but usually requires replicate data in order to avoid the costly data redistribution operations. Object-space parallel does not require data redistribution or replication, so this type of parallelism has better storage scalability as the data size increases. However, since the intensity of each pixel may originate from several CPUs, the composition of the final image requires a great deal of communication. The communication overhead will increase greatly with the increase in the CPU number.

Obviously, on distributed-memory machines, object-space parallel is better for very large datasets to avoid the memory problem, and the image-space parallel is better for shared-memory machines. However, for the Earth Simulator, the hybrid architecture provides a very good opportunity to take advantage of both parallel methods. Object-space parallel can be used among SMP nodes in order to reduce the data size on each SMP node, and image-space parallel is used in each SMP node to take advantage of its shared memory. Therefore, we developed a hybrid-space PVR method, which can avoid the storage problem for large datasets, the communication bottleneck for large numbers of CPUs, and obtain a good load balance in each SMP node.

*(2) Optimization in parallel programming model: Three-level hybrid parallelization*

The Earth Simulator has a hierarchical memory architecture with distributed memory for each node and shared memory among the CPUs in each node. On the distributed machines, MPI is used for message passing among CPUs. For SMP cluster machines, it is still available to just use MPI for message passing by regarding all the CPUs with independent memory and neglecting the shared memory among the CPUs in the same node.

However, in order to make full use of the hybrid memory architecture on the Earth Simulator, the *loop directives + message passing* style *hybrid* programming model appears to be effective when a message passing technique such as MPI is used in inter-SMP node communication, and when intra-SMP node parallelization is guided by thread parallel, which can take advantage of the shared memory available within SMP nodes. Furthermore, vectorization is performed in each CPU.

#### 4.2.2 High Image Quality

Since large scale simulation requires higher visualization quality, we adopted some traditional techniques in the PVR module to improve the quality of the image.

For example, in order to account for the large dynamic range of the seismic wavefield, the amplitude of the wavefield is compressed using a logarithm function. A low opacity (large transparency) is assigned to grid points of large wavefield amplitude, and relatively high opacity is assigned to weak wavefield. This highlights the outline of the seismic wavefield clearly, and prevents small, scattered waves from obscuring important features.

Data distribution is often very non-uniform, so a good color mapping method is very important for visualization quality. Our PVR module not only provides very convenient ways for users to define nonlinear color mapping, but also provides an automatic, best color mapping style which is based on the inverse histogram transform of the data distribution. Users need only to select the automatic color mapping style, and then the visualization image with the best color mapping effects will be generated automatically.

In order to improve the quality of volume rendering, we have developed many opacity transfer functions which are convenient for users to define suitable transfer functions, such as emphasizing high gradient regions, highlighting feature data intervals, proportional or inversely proportional to the distance from the view point, proportional or inversely proportional to the data value, and so on.

The PVR module runs on the Earth Simulator at almost comparable speed to the main FDM calculation. For example the visualization of $512\times256\times512$ model and the image resolution of $640\times480$ took about 10 s using 16 nodes of the Earth Simulator. Examples of volume visualization are shown in Figs. 7, 11 and 12.

## 5 Parallel Simulation of Long-Period Surface Waves from the 2000 Tottori-ken Seibu ($M_J$7.3) Earthquake

A numerical simulation of seismic wave propagation during the 6 Oct. 2000 Tottori-ken Seibu earthquake ($M_J$ 7.3) in Japan was performed to examine the effectiveness of the proposed scheme for large-scale simulations. A detailed structural model of the crust and upper mantle was used in conjunction with the source rupture model

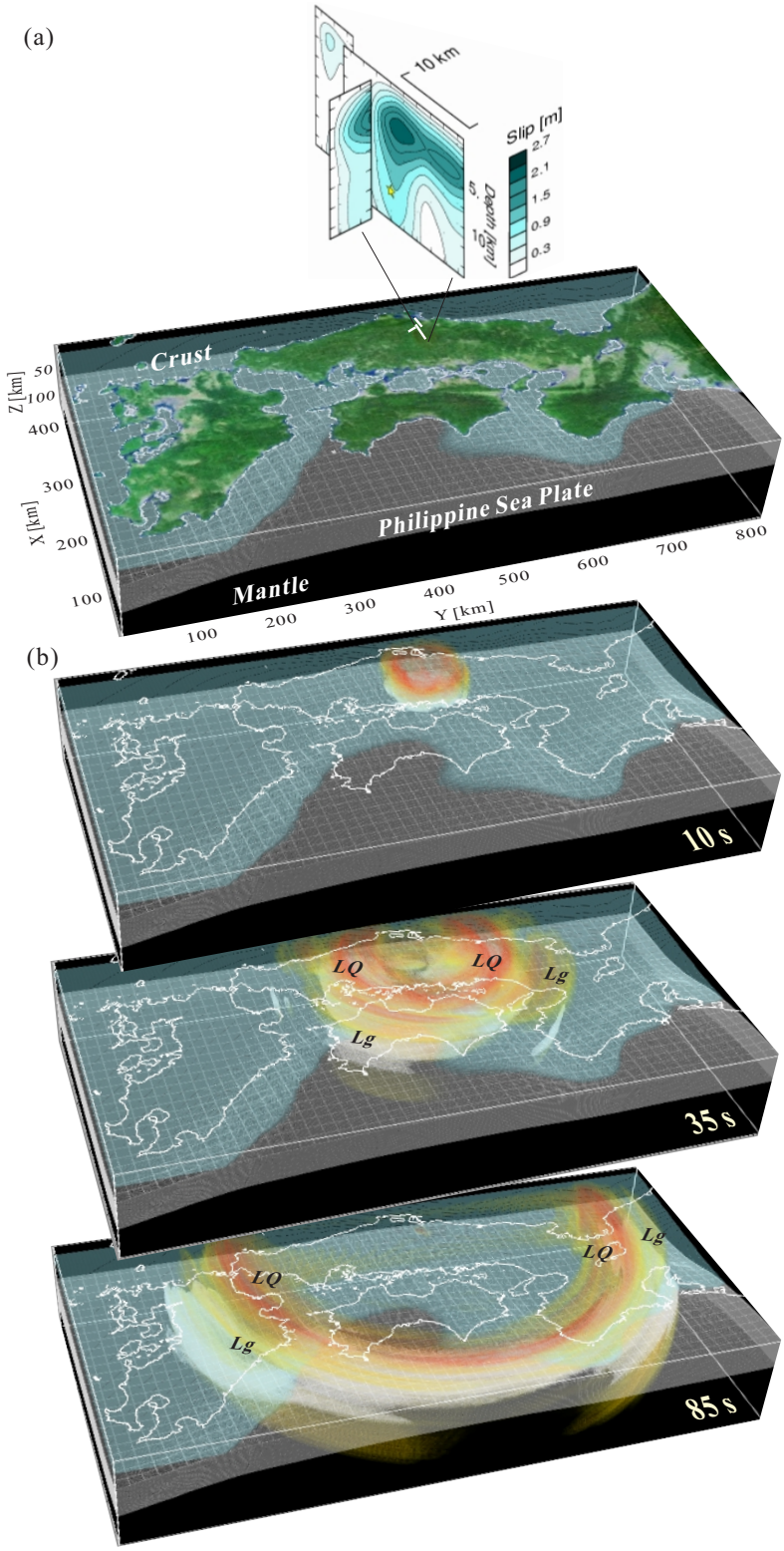


**Figure 7** : (a) Structural model of western Japan used in the 3D simulation of seismic waves, showing the configuration of crust and upper-mantle structures and the Philippine-Sea Plate. The source-slip model of Yagi and Kikuchi (2000) for the 2000 Tottori-ken Seibu earthquake is shown at the top. (b) Snapshots of wave propagation 10 s, 35 s, and 85 s after source initiation. Major crustal S wave (*Lg*) and the fundamental mode Love wave (*LQ*) are marked.

for the earthquake.

The ground motions during this event were well recorded by 521 K-NET and KiK-net stations on a regional scale, making it possible to confirm the characteristics in the wavefield during the earthquake quite clearly. The most notable feature of the seismic wavefield of this earthquake was the large amplitude of the surface wave (Love wave) with long dominant period of about 10 s and relatively low speed of about 2.7 km/s.

### 5.1 Simulation Model for Western Japan

The simulation model represents a 820 km by 410 km area and extends to a depth of 128 km. The model is discretized into elements with dimensions of 0.4 km by 0.4 km in the horizontal direction and 0.2 km in the vertical direction embedded over a base model of 0.8 km (horizontal) by 0.4 km (vertical). The subsurface structure model of western Japan is constructed based on refraction experiments [e.g., Yoshii, Sasaki, Tada, Okada, Asano, Muramatu, Hashizume, and Moriya (1974)] and P-wave travel-time tomography studies [Zhao and Hasegawa (1993)] as listed in Tab. 3. The 3D model includes lateral changes in the Moho depth [Ryoki (1999)] and depth of the Philippine-Sea Plate [Yamazaki and Ooida (1985)].

The area of the simulation is almost the same as that used in the previous experiment [Furumura, Kennett, and Koketsu (2003)] using coarse grid models (0.8 km $\times$ 0.8 km $\times$ 0.4 km; 1.6 km $\times$ 1.6 km $\times$ 0.8 km) and higher velocities ($V_S = 2.1$ km/s) in the sedimentary basins. However, the finer model used in the present simulation provides a more realistic wave propagation model for frequencies as low as 1 Hz even when using realistic lowered velocities of $V_S = 1.2$ km/s in the basins.

The source model of Yagi and Kikuchi (2000) was used, which was derived by inversion using the K-NET and KiK-net records and teleseismic waveforms. The inferred slip distributions on the fault planes are shown in the upper part of Fig. 7(a). The slip model is represented by a large ($> 2$ m), shallow ($< 4$ km) strike-slip fault above the epicenter. In the simulation model, the source rupture is represented by a set of point sources arranged on the fault plane, generating a seismic wave with maximum frequency of 1 Hz and total seismic moment of $M_o = 1.9 \times 10^{19}$ Nm.

### 5.2 Parallel Simulation of the 2000 Tottori-ken Seibu Earthquake

The 3D model is partitioned vertically into 32 subdomains of equal grid numbers, and each subdomain is assigned to the same number of nodes of the Earth Simulator. Seismic wave propagation is then calculated by solving the equations of motion using the 16th-order centered staggered-grid FDM in the horizontal $(x, y)$ direction, and a 4th-order staggered-grid FDM in the vertical $(z)$ direction. MPI is used for inter-processor communications at each time step. The parallel simulation used 100 Gbyte of memory with a total CPU time of about 20 min in parallel computation using 32 nodes (256 CPUs) of the Earth Simulator.

### 5.3 Comparison between Simulation and Observations

Figure 7 shows a set of snapshot of the 3D parallel seismic wavefield generated by simulation and concurrent visualization on the Earth Simulator.

The shallow strike-slip fault source of the Tottori-ken Seibu earthquake radiated large SH waves in the crust, which can be clearly seen in the first frame ($T = 35$ s) as a four-lobe pattern of seismic wave propagation around the source. In the next two frames (35 s and 85 s), the development of the fundamental-mode Love ($LQ$) wave by multiple reflection in the crust can also be clearly seen. The $LQ$ wave propagation in western Japan occurs at a relatively low wave speed of about 2.7 km/s, together with a weak but faster $Lg$ waves of about 3.5–2.8 km/s.

A snapshot of simulated horizontal ground motion is shown in Fig. 8(a), to be compared with the observed wavefield in Fig. 8(b). There is a good correlation between the observations and the simulation, except for a slight underestimation of the amplitude of surface waves. The effect of deep basin structures in major population centers such as Nagoya, Osaka, and Oita can also be clearly seen as regions of significant amplification and extension of long-period waves. Such localized amplification effects due to deep, low-velocity ($V_S = 1.2$ km/s) structures are clearly demonstrated in this simulation using a high-resolution ($0.4 \times 0.4 \times 0.2$ km) mesh model, whereas previous simulations using coarser ($0.8 \times 0.8 \times 1.6$ km) mesh models and higher velocities for the basin could not reproduce this feature [Furumura, Kennett, and Koketsu (2003)]. However, slight underestimation of the

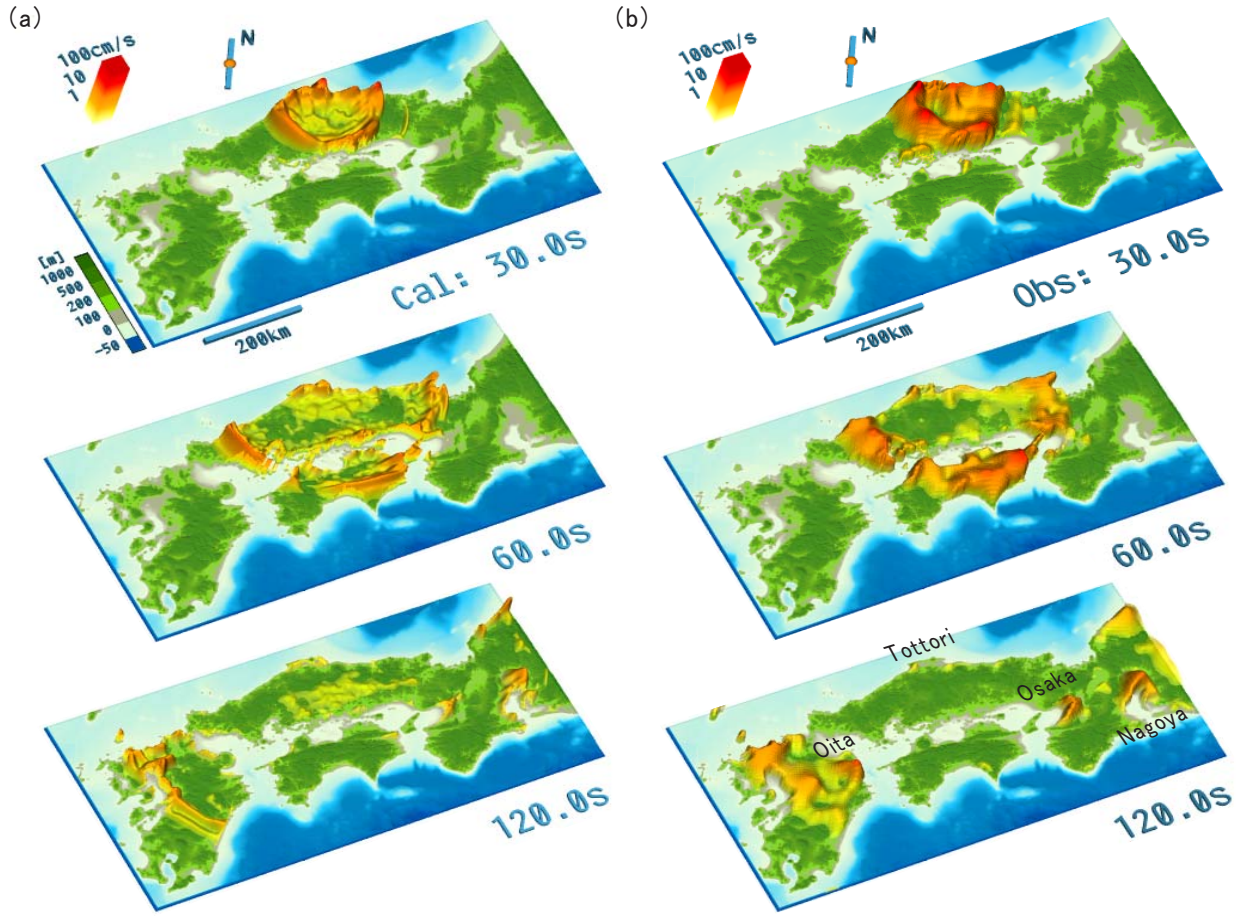


**Figure 8** : Comparison of (a) simulated and (b) observed ground motions for the 2000 Tottori-ken Seibu earthquake. Amplitude of ground velocity motions is in units of cm/s, scale bar is shown in the 3D view.

**Table 3** : Base model of crust and upper mantle in western Japan used in the simulation.

| | Thickness (km) | $V_P$ (km/s) | $V_S$ (km/s) | ρ (t/m$^3$) | $Q_P$ | $Q_S$ |
|---|---|---|---|---|---|---|
| Layer 1 (Sediment) | <2.0 | 2.20 | 1.20 | 1.8 | 160 | 80 |
| Layer 2 | 2.0 | 4.00 | 2.10 | 2.0 | 200 | 100 |
| Layer 3 | 3.0 | 5.60 | 3.23 | 2.0 | 400 | 200 |
| Upper Crust | 13.0 | 6.00 | 3.46 | 2.5 | 600 | 300 |
| Lower Crust | 14.0 | 6.60 | 3.82 | 2.7 | 800 | 400 |
| Upper Mantle | 40.0 | 7.80 | 4.50 | 3.0 | 1000 | 500 |
| | —— | 8.00 | 4.62 | 3.2 | 1000 | 500 |

surface wave such as at Oita basin (see 120 s frame) indicating the incompleteness of amplification effects in the shallow layer which can not include even in the current small-mesh model.

## 6 Parallel Simulation of High-Frequency Waves during the 1993 Kushiro-oki Earthquake ($M_J$ 7.8)

Deep-focus earthquakes occurring in the subduction zone of the Pacific Plate, always displays anomalous extension of isoseismic contours from the hypocenter out to

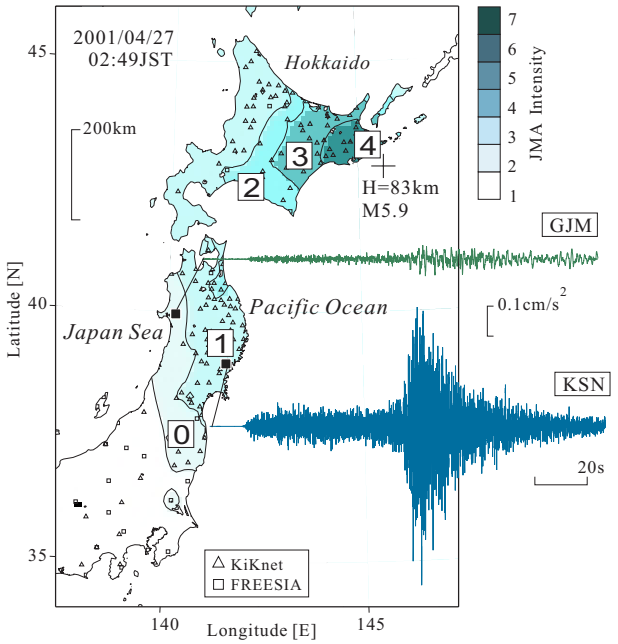


**Figure 9** : An example of anomalous intensity pattern for a deep plate earthquake in Hokkaido and comparison of broadband acceleration waveforms obtained at two stations (GJM and KSN) located at almost equal distances from the source.

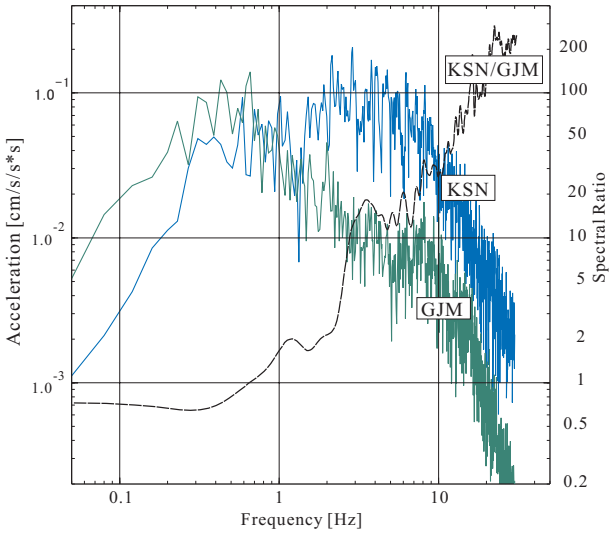


**Figure 10** : Spectral ratio of S waveforms at stations KSN and GJM for a recent earthquake (April 27, 2001; Fig. 9). The spectral ratio of the Fourier spectrum of KSN relative to GJM for the earthquake is also shown (thick line).

several hundred kilometers to the south along the eastern seaboard (Pacific Ocean side). The intensity decays significantly in the inland direction and along the western seaboard (Japan Sea side). Such large-scale anomalies are expected to be caused by the variation in large-scale structure of the crust and upper mantle in the subduction zone rather than by localized site amplification effects such as in sedimentary basins.

The anomalous intensity observed in northern Japan during deep plate earthquakes has been studied extensively by Utsu (1966) and Utsu (1967) as a cause of lateral variation in the absorption structure in the seismic zone (subduction plate) and its surrounding mantle (mantle wedge). Utsu and Okada (1968) explained, based on an analysis of the waveforms at inland and eastern stations, that the attenuation coefficients ($Q$) for the subduction plate must be at least ten times larger than those for the surrounding mantle in order to explain the observed intensity distribution.

### *6.1 Anomalies Intensity Pattern for Deep Plate Earthquakes*

Fig. 9 shows an example of such an anomalous intensity distribution for a recent earthquake (27 Apr. 2001; $H =$ 83 km, $M_J$ 5.9) near the coast of Kushiro in Hokkaido. A large number of waveforms were available from K-NET and KiK-net records, and these couples with a FREESIA broadband waveform of NIED were used to derive a detailed seismic intensity map.

The intensity distribution during this earthquake clearly reveals anomalous extension of isoseismic contours from the source toward the south for several hundred kilometers along the eastern coast of the Pacific Ocean, whereas the intensity decays significantly toward inland and along the coast on the Japan Sea side. The seismic intensity is characterized by higher-frequency ground oscillations of 0.5 Hz to higher than 5 Hz, indicating the difference in the absorption characteristics for high-frequency waves in the crust and upper mantle in the subduction zone.

The large observed intensities of the high-frequency waves along the Pacific Ocean can also be clearly confirmed by comparison of the broadband waveforms at KSN and GJM, located at similar distances from the source (Fig. 9), with the Fourier spectrum of the acceleration waveforms shown in Fig. 10. There is a marked dif-

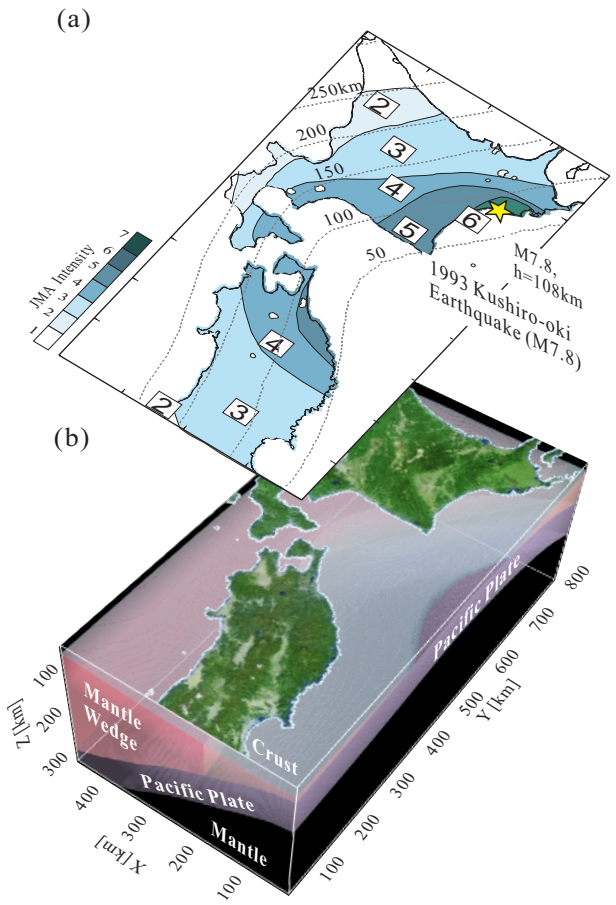


**Figure 11** : (a) Anomalous seismic intensity distribution from source toward the south during the 1993 Kushiro-oki ($M_J$ 7.8) earthquake. (b) 3D model of the subduction structure beneath northern Japan used in the simulation. The depth of the subducting plate is shown at the top.

ference between the amplitudes of high-frequency waves (>2 Hz), and this difference increases rapidly with increasing frequency.

### 6.2 *High-frequency simulation of the 1993 Kushiro-oki Earthquake ($M_J$ 7.8)*

In order to investigate the process giving rise to the higher intensities along the subducting Pacific Plate, high-frequency simulations of seismic waves were conducted for the 1993 Kushiro-oki earthquake ($M_J$ 7.8), which occurred at a depth of $H = 108$ km close to the earthquake mentioned above. The seismic intensity of the 1993 event based on Japan Meteorological Agency (JMA) station records is shown in Fig. 11(a). The anomalous intensity pattern can also be seen very clearly for this event.

#### 6.2.1 *Simulation Model*

The 3D model is 820 km by 410 km horizontally, and extends to a depth of 300 km. The model is discretized at a uniform grid size of 0.4 km (horizontal) by 0.2 km (vertical). The velocity and attenuation structures are the same as those used in the simulation of western Japan (Tab. 3), with 5% higher velocities for the P and S waves and higher quality factors ($Q_P = 1000$, $Q_S = 500$) for the Pacific Plate following the study of Zhao and Hasegawa (1993). Slightly lower (5%) P and S wave velocities and lower quality factors ($Q_P = 200$, $Q_S = 100$) were assigned to the mantle wedge. The depth of the subducting Pacific Plate is as reported by Kosuga, Sato, Hasegawa, Matsuzawa, Suzuki, and Motoya (1996), and the thickness of the plate is set at 80 km. The depth of the crust/mantle boundary (Moho interface) was derived from a tomography study by Zhao and Hasegawa (1993) based on P- and S-wave travel-time data.

A minimum shear wave velocity of 3.2 km/s is assigned to the superficial layer, allowing the simulation of seismic waves with higher-order FDM to treat seismic waves at frequencies below 3 Hz by sampling at 2.7 and 5.4 grid points per shortest wavelength in the horizontal and vertical directions, respectively.

As the main goal is to understand the contribution of each class of heterogeneity in the crust and upper mantle to the propagation of high-frequency seismic waves, the large fault source was approximated as a simple point source. The seismic source of the normal fault event (dip $= 6°$, strike = N133°E, rake $= -36°$) generated a seismic wave with frequencies of up to 3 Hz and a seismic moment of $Mo = 3.3 \times 10^{22}$ Nm for the $M_J$ 7.8 event.

A 3D simulation of 31 billion-element model used 0.5 Tbyte of memory and took approximately 2 h for parallel computation using 128 nodes (1024 CPUs) of the Earth Simulator.

#### 6.2.2 *Simulation Results*

A set of simulations were conducted using different structural models, each including a part of the subduction zone model (subduction plate, mantle wedge, etc.), in order to understand the contribution of each model to the anomalous propagation and attenuation of high-frequency waves in the subduction zone.

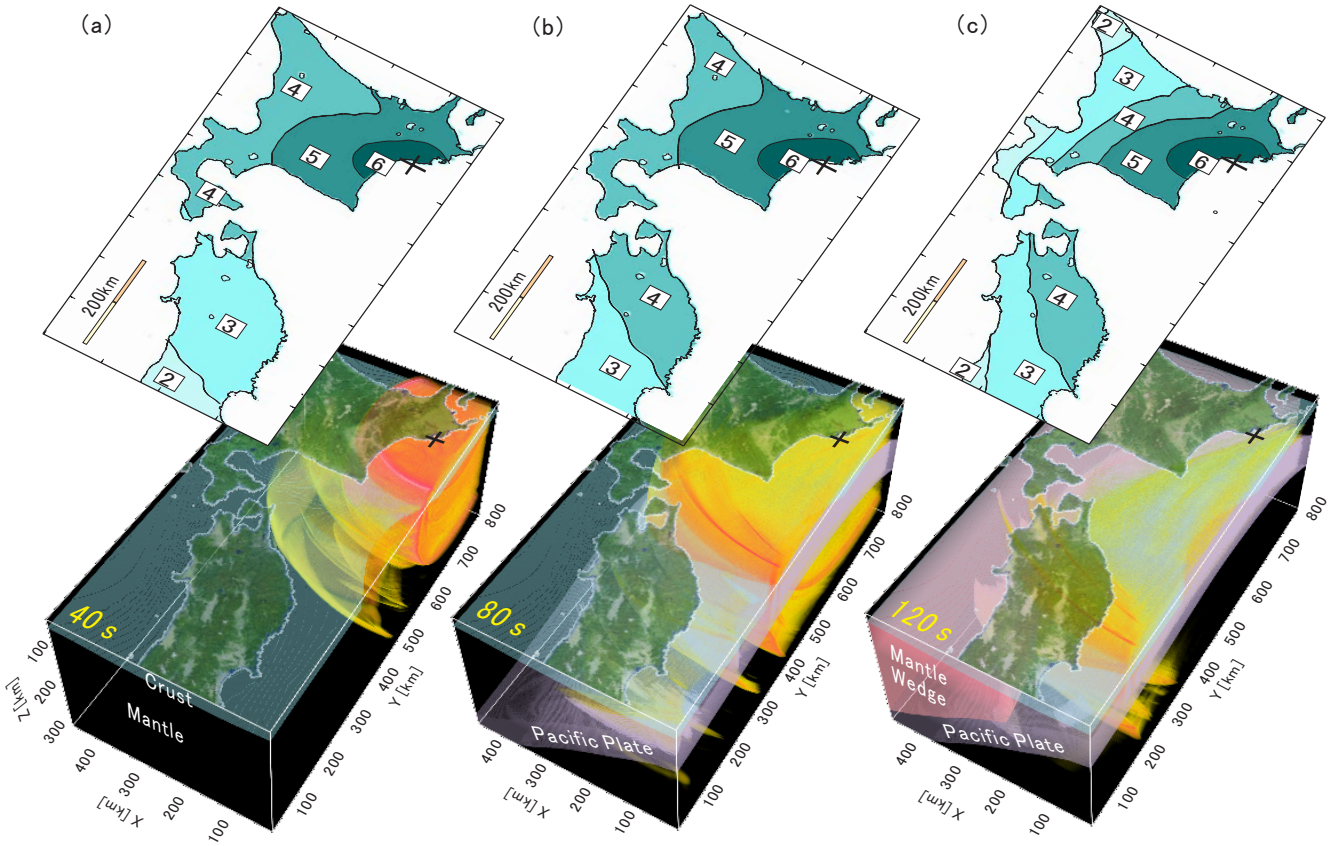


**Figure 12** : Snapshot of 3D wavefield from simulation of the 1993 Kushiro-oki earthquake with (a) laterally heterogeneous crust, (b) the inclusion of the high-$Q$ Pacific plate, and (c) the incorporation of a full subduction zone model including the Pacific plate and the low-$Q$ mantle wedge. The pattern of intensities derived from these simulations are shown at the top.

The first simulation treated a laterally heterogeneous crustal structure, excluding heterogeneities imposed by the subducting plate and the mantle wedge. The simulation produced an isoseismal pattern of seismic intensity above the hypocenter [Fig. 12(a)]. By introducing the high-velocity subducting plate and low-attenuation oceanic mantle, a clear extension of intensity contours emerged from the hypocenter toward the south along the eastern seaboard [Fig. 12(b)]. Incorporation of the low-velocity and high-attenuation mantle wedge significantly attenuates seismic waves propagating inland and along the western seaboard of the Japan Sea [Fig. 12(c)].

The enhanced seismic intensity anomalies in Fig. 12(c) reproduced the observations of the 1993 Kushiro-oki earthquake (Fig. 11) well. The radiation of seismic P and S waves from the deep earthquake, with efficient propagation of seismic waves along the plate and attenuation in the mantle wedge, is clearly shown in the snapshots of the 3D wavefield shown in Fig. 12.

## 7 Conclusion

The characteristics of the regional wavefield is controlled significantly by the radiation properties of the seismic source and the structural variations in the crust and upper mantle along the propagation path. This study also confirmed that complex seismic behavior resulting from heterogeneities can be reproduced by large-scale, fine-mesh simulation on the Earth Simulator and suitable visualization techniques for the 3D wavefield, and can be compared with high-resolution seismic observations by K-NET and KiK-net across Japan.

The complex regional seismic wavefield in Japan was reproduced by applying the developed scheme to two examples; the 2000 Tottori-ken Seibu earthquake, and the 1993 Kushiro-oki earthquake. The results of the simulations agree with the general characteristics of observa-

tions. The next objective for our group is to apply the proposed simulation model to investigation of the pattern of ground motions expected for future earthquakes. Improvement in the accuracy of prediction of strong ground motions will depend on maintaining the close correlation between the observations and computer simulations.

**Acknowledgement:** This study was conducted as part of a joint research project with the Earth Simulator Center in 2003 under the title "Numerical simulation of seismic wave propagation and strong ground motions in 3D heterogeneous media". The authors acknowledge the Earth Simulator Center and Supercomputer Center of the University of Tokyo for providing computer resources. Figures were drawn using the POV-Ray rendering software developed by C. Cason and the GMT software developed by P. Wessel and W.H.F. Smith. K-NET, KiK-net, and FREESIA data are available on the NIED website (http://www.bosai.go.jp).

## References

**Aoi, S.; Fujiwara, H.** (1999): 3-D finite-difference method using discontinuous grids computational mechanics. *Bull. Seism. Soc. Am.*, vol. 89, pp. 918–930.

**Cerjan, C.; Kosloff, K.; Kosloff, R.; Reshef, M.** (1985): A nonreflecting boundary condition for discrete acoustic and elastic wave equation. *Geophysics*, vol. 50, pp. 705–708.

**Chen, L.; Fujsihiro, I.; Nakajima, K.** (2003): Optimizing parallel performance of unstructured volume rendering for the earth simulator. *Parallel Computing*, vol. 29, pp. 355–371.

**Furumura, T.; Kennett, B.; Koketsu, K.** (2003): Visualization of 3D wave propagation from the 2000 Tottoriken Seibu, Japan Earthquake: Observation and numerical simulation. *Bull. Seism. Soc. Am.*, vol. 93, pp. 870–881.

**Furumura, T.; Kennett, B.; Takenaka, H.** (1998): Parallel 3-D pseudospectral simulation of seismic wave propagation. *Geophysics*, vol. 63, pp. 279–288.

**Furumura, T.; Koketsu, K.; Wen, K.-L.** (2002): Parallel PSM/FDM hybrid simulation of ground motions from the 1999 Chi-Chi, taiwan, earthquake. *Pure and Applied Geophysics*, vol. 159, pp. 2130–2146.

**Graves, R.** (1996): Simulating seismic wave propagation in 3-D elastic media using staggered-grid finite differences. *Bull. Seism. Soc. Am.*, vol. 86, pp. 1091–1106.

**Hatzigeorgiou, G.; Beskos, D.** (2002): Dynamic response of 3-D damaged solids and structures by BEM. *CMES: Computer Modeling in Engineering & Sciences*, vol. 3, pp. 791–802.

**Hestholm, S.** (1999): Three-dimensional finite difference viscoelastic wave modeling including surface topography. *Geophys. J. Int.*, vol. 139, pp. 852–878.

**Kinoshita, S.** (1998): Kyoshin Net (K-NET). *Seism. Res. Lett.*, vol. 69, pp. 309–332.

**Kosuga, M.; Sato, T.; Hasegawa, A.; Matsuzawa, T.; Suzuki, S.; Motoya, Y.** (1996): Spatial distribution of intermediate-depth earthquakes with horizontal of vertical nodal planes beneath northeastern Japan. *Phys. Earth and Planet. Int,*, vol. 93, pp. 63–89.

**Levoy, M.** (1988): Display of surfaces from volume data. *IEEE CG&A*, vol. 8, pp. 29–37.

**Olsen, K.; Archuleta, R.; Matares, J.** (1995): Three-dimensional simulation of a magnitude 7.75 earthquake on the San Andreas fault. *Science*, vol. 270, pp. 1628–1632.

**Reshef, M.; Kosloff, D.; Edwards, M.; Hsiung, C.** (1988): Three dimensional acoustic modeling by the Fourier method. *Geophysics*, vol. 53, pp. 1175–1183.

**Ryoki, K.** (1999): Three-dimensional depth structure of the crust and upper-most mantle beneath Southwestern Japan and its regional gravity anomalies. *Zishin 2*, vol. 52, pp. 51–63.

**Sellountos, E.; Polyzos, D.** (2003): A MLPG (LBIE) method for solving frequency domain elastic problems. *CMES: Computer Modeling in Engineering & Sciences*, vol. 4, pp. 619–636.

**Sladek, J.; Sladek, V.; Zhang, C.** (2003): Application of meshless local Petrov-Galerkin (MLPG) method to elastodynamic problems in continuously nonhomogeneous solids. *CMES: Computer Modeling in Engineering & Sciences*, vol. 4, pp. 637–648.

**Smith, W.; Wessel, P.** (1990): Griding with continuous curvature splines in tension. *Geophysics*, vol. 55, pp. 293–305.

**Utsu, T.** (1966): Regional difference in absorption of seismic waves in the upper mantle as inferred from abnormal distribution of seismic intensities. *J. Fac. Sci. Hokkaido Univ, Ser VII*, vol. 2, pp. 359–374.

**Utsu, T.** (1967): Anomalies in seismic wave velocity and attenuation associated with a deep earthquake zone (I). *J. Fac. Sci. Hokkaido Univ, Ser VII*, vol. 3, pp. 1–25.

**Utsu, T.; Okada, H.** (1968): Anomalies in seismic wave velocity and attenuation associated with a deep earthquake zone (II). *J. Fac. Sci. Hokkaido Univ, Ser VII*, vol. 3, pp. 65–84.

**Yagi, Y.; Kikuchi, M.** (2000): Source rupture process of the tottori-ken seibu earthquake of Oct. 6, 2000, (Mjma 7.3) by using joint inversion of far-field and near-field waveform. *Abst. Seism. Soc. Japan 2000 Fall Meet.*, pg. T04.

**Yamazaki, F.; Ooida, T.** (1985): Configuration of subducted Philippine Sea plate beneath the Chubu distinct, central Japan. *Zishin 2*, vol. 38, pp. 193–201.

**Yoshii, T.; Sasaki, Y.; Tada, T.; Okada, H.; Asano, S.; Muramatu, I.; Hashizume, I.; Moriya, T.** (1974): The third Kurayoshi explosion and the crustal structure in western part of Japan. *J. Phys. Earth*, vol. 22, pp. 109–12.

**Zhao, D.; Hasegawa, A.** (1993): P wave tomographic imaging of the crust an upper mantle beneath the Japan islands. *J. Geophys. Res*, vol. 98, pp. 4333–4353.